This article has been accepted for publication in a future issue of this journal, but has not been fully edited. Content may change prior to final publication. Citation information: DOI 10.1109/TPEL.2017.2765355, IEEE Transactions on Power Electronics

Adaptive Commutation Error Compensation Strategy Based on a Flux Linkage Function for Sensorless Brushless DC Motor Drives in a Wide Speed Range

Shaohua Chen, Xiangyu Zhou, Guochang Bai, Kun Wang and Lianqing Zhu

***Abstract*—This paper presents a novel adaptive commutation error compensation strategy for the sensorless brushless DC (BLDC) motor based on the flux linkage function. It addresses the two key challenge problems on the sensorless control of the BLDC motor. The one is presenting a novel detection method for the BLDC motor rotor position signal to filter out the interference and the noise by the high frequency. The other one is proposing a commutation error compensation strategy to improve the system efficiency. In traditional sensorless control strategy, a deep low pass filter is usually used to obtain the BLDC motor rotor position signal from the high frequency interference. However, the delayed angle caused by the low pass filter may be more than 90 electrical degrees in the high speed range. Therefore, a novel sensorless control strategy based on the speed–independent flux linkage function was proposed in this paper. The interference of the diode freewheeling was filtered by the software filter, and a closed–loop compensation algorithm based on the deviation of line–to–line voltages was illustrated to correct the commutation error in the high speed range. The stability and accuracy of the method was confirmed by a series of experiments.**

***Index Terms*—BLDC motor, sensorless control strategy, flux linkage function, commutation error.**

I. INTRODUCTION

BLDC motor, which is widely used in the scientific instruments and the industrial equipment, has the advantages of simple structure and high efficiency [1]–[2]. The rotor position is one of the most important parameters for the BLDC motor three–phase six–state control strategy. The hall sensor, photoelectric encoder and resolver are usually used to provide the BLDC motor commutation information. However, the sensor detection accuracy is easily influenced by the external environment and the installation precision [3]–[4]. Therefore, the research of the sensorless driving of the BLDC motor has great significance both for the industrial applications and the scientific research [5]–[7].

The two research interests of sensorless, which are the detection of the rotor position in the low speed range and the high precision commutation error compensation in the high speed range, attract the attention of many scholars [8]. For the first interest, a novel sensorless start–up strategy for a high–speed 100 kW BLDC motor based on the voltage comparator was proposed in [1]. And a low pass filter was used to filter out the interference and the noise by the high frequency in the low speed range. It is difficult to correct the delayed angle caused by the low pass filter. The flux linkage function can be used to detect the BLDC rotor position information in the low speed range [35]. However, the flux linkage function was easily to be affected by the interference and the noise by high frequency. A minimum current start–up strategy of a permanent–magnet synchronous motor (PMSM) was proposed in [9]. In this method, only one current sensor was used to estimate the rotor position information, which reduces the motor driver loss. The research in [10]–[12] proposed a sensorless start–up method for the PMSM based on the flux linkage function. And the rotor position information can be detected at the standstill status by the proposed method. Nevertheless, there are some problems in this method when used for the BLDC motor with the surface–mounted rotor structure. The research in [13]–[15] proposed a "three–step startup" control strategy based on the motor back electromagnetic force (back–EMF). The rotor position information cannot be detected in the low speed range, and the high synchronization switching speed may cause other problems. For the second interest, a sensorless commutation error compensation strategy for a 100 kW high–speed BLDC motor was proposed [16]. And the variations of the phase voltage before and after the commutation can be used as the feedback signal to compensate the commutation error. The sensorless control strategy based on the back–EMF was very

Manuscript received May 15, 2017; revised Jul 4, 2017 and Sep 14, 2017; accepted Oct 18, 2017. This work was supported in part by the Cultivation and Development Project of Science and Technology Innovation Base of Beijing under Grant Z131104002813105, in part by the Innovation Capacity Improvement Project of Beijing Municipal Commission of Education under Grant TJSHG201510772016, in part by the Opening Foundation of Beijing Engineering Research Center under Grant GD2017008. (Corresponding authors: G. Bai, K. Wang and L. Zhu)

S. Chen, X. Zhou and L. Zhu are with the School of Instrument Science and Opto-electronics Engineering, Beijing Information Science and Technology University, Beijing, China S. Chen, X. Zhou and L. Zhu are also with the Beijing Engineering Research Center of Photoelectric information and instrument, Beijing 100192, China, S (e-mail: buaa38605@sina.com, 925154232@qq.com, zhulianqing@sina.com).

G. Bai is with the School of Mechanical Engineering. Zhengzhou University, Zhengzhou, China (e-mail: 13611291762@126.com).

K. Wang is with the School of Instrumentation Science and Opto-electronics Engineering. Beihang University, Beijing, China (e-mail: wangkunggg@163.com).

0885-8993 (c) 2017 IEEE. Personal use is permitted, but republication/redistribution requires IEEE permission. See http://www.ieee.org/publications_standards/publications/rights/index.html for more information.

This article has been accepted for publication in a future issue of this journal, but has not been fully edited. Content may change prior to final publication. Citation information: DOI 10.1109/TPEL.2017.2765355, IEEE Transactions on Power Electronics

sensitive to the back–EMF shape [17]. The influence of the noni–deal back–EMF and the detection circuit was analyzed in [18]–[19]. The proposed method based on the overcurrent and the overvoltage in [20] can achieve an effective compensation effect in wide speed range. However, the method did not analyze the commutation error caused by the low pass filter in the high speed range. An improved method for the rotor position signal detection from zero sequence voltage was proposed in [21]. The flat group delay error of Bessel low–pass filters was analyzed detailed in the proposed method. And it can be used to drive the BLDC motor with a non-ideal back-EMF from low starting speed (3.3 % of the rated speed) to the high speed range. The research in [22] proposed a novel commutation error compensation strategy for a BLDC motor based on the DC–link current. An improvement sensorless control strategy based on the analyzing of the back–EMF was proposed in [23]. The system efficiency can be increased by accurate commutation. S. Yang et al. [24] proposed a novel sensorlees method to improve the speed range of the BLDC motor. Two control modes were described to detect the rotor position information in the low speed range and the high speed range separately. The research in [25]–[27] proposed an interesting sensorless BLDC motor control strategy, and a G function was defined to estimate the rotor position. Because the G function is independent with the motor speed, it can be used in the wide speed rang in theory. However, a lot of data collection and calculation are needed to estimate the rotor position in real time because of high frequency Pulse–Width Modulation (PWM), and it is very difficult to extract the rotor position signal from the interference and the noise caused by the high frequency PWM signal.

The researches in [28]–[31] presented some methods to compensate the commutation errors for the BLDC motors in real time. In [28], a novel compensation strategy based on the neutral voltage to estimate the rotor position was proposed. A trapezoidal back–EMF waveform was required, and the designing of the PI regulator parameters was relied on the load torque in the proposed technique. The researches in [29]–[30] proposed a control strategy to compensate commutation errors based on the off–line compensation method. The proposed method is simple and very practical. However, the real–time performance is poor and cannot respond quickly to the load torque change. With the arguments above, few control algorithms were able to realize the real time commutation compensation in the wide speed range. Therefore, a simple sensorless control strategy for the BLDC motor driver should be studied to compensate the commutation error in the whole speed range.

This paper introduced a novel sensorless control strategy of BLDC motor for the petroleum drilling system based on a speed–independent flux linkage function. Two key problems are solved: an optimized G function was proposed to detect the rotor position information and compensate the commutation error in real time. The commutation error can be calculated by the integral deviation of the terminal voltage. The commutation error compensation was based on the commutation threshold adjustment, and the optimal commutation point can be estimated from the extreme point of G function in real time. The specific content arrangement in this paper is as follows. The analyses of rotor position estimation based on traditional G function are described in Section II. The influence of the rotor position detection based on the optimized G function and the influence of the motor commutation error on the motor terminal voltage are present in Section III. A novel sensorless closed–loop control system for the BLDC motor is shown in Section IV. The experimental evaluations are present in Section V. Finally, conclusions and outlook can be found in Section VI..

II. Sensorless Commutation Algorithm Based on the Traditional G Function

A. Mathematical model of the BLDC motor

Generally, a buck converter is usually used to reduce the torque ripple in BLDC motor driver [32]–[34]. In this topology, the Pulse Amplitude Modulation (PAM) control strategy of the inverter for BLDC motor is used. Therefore, the inverter topology based on the buck converter of BLDC motor can be shown in Fig. 1.

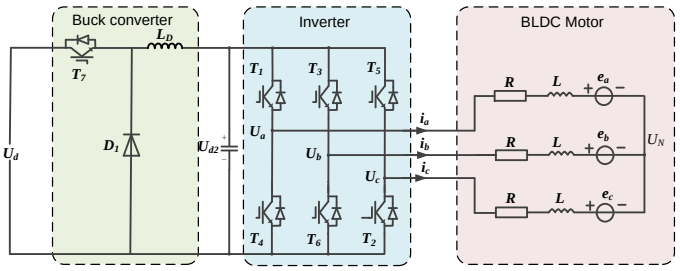

Fig. 1. The inverter topology based on a buck convertor.

Where U_d is the bus voltage, T_7 is the switch of buck converter, D_1 is the freewheeling diode, L_D is the inductance of buck converter, U_{d2} is the output voltage of the buck converter, U_a, U_b, and U_c are the phase voltages, i_a, i_b, and i_c are the phase currents, R is the phase resistance, L is the phase inductance, e_a, e_b, and e_c are the back EFMs, U_N is the voltage of neutral point.

The line–to–line voltages equations of the BLDC motor are as follows:

$$\begin{cases} U_{ab} = R(i_a - i_b) + L\dfrac{d(i_a - i_b)}{dt} + k_e\omega\dfrac{d(f_{abr}(\theta))}{d\theta} \\ U_{bc} = R(i_b - i_c) + L\dfrac{d(i_b - i_c)}{dt} + k_e\omega\dfrac{d(f_{bcr}(\theta))}{d\theta} \\ U_{ca} = R(i_c - i_a) + L\dfrac{d(i_c - i_a)}{dt} + k_e\omega\dfrac{d(f_{car}(\theta))}{d\theta} \end{cases} \quad (1)$$

where $f_{xyr}(\theta)$ is the flux linkage function of the rotor position, k_e is the coefficient of back–EMF. The relationship between the back–EMF and the phase currents in one cycle is shown in Fig. 2.

The zero-crossing points of line–to–line back–EMFs can be detected by the detection circuit, and it corresponds to the commutation points.

0885-8993 (c) 2017 IEEE. Personal use is permitted, but republication/redistribution requires IEEE permission. See http://www.ieee.org/publications_standards/publications/rights/index.html for more information.

This article has been accepted for publication in a future issue of this journal, but has not been fully edited. Content may change prior to final publication. Citation information: DOI 10.1109/TPEL.2017.2765355, IEEE Transactions on Power Electronics

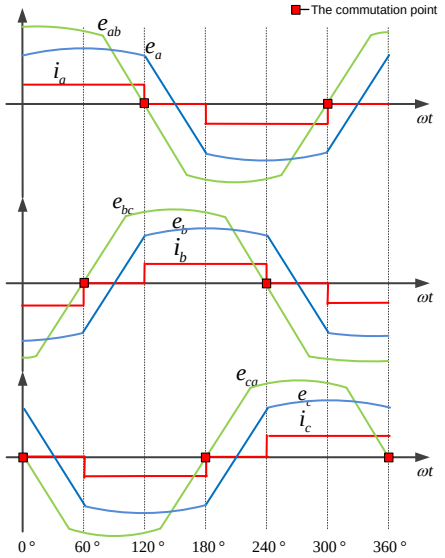

Fig. 2. The relationship between the back EMF and the phase currents waveforms.

B. *The traditional G function*

The flux linkage function can be given as follows:

$$\begin{cases} \dfrac{d(f_{abr}(\theta))}{d\theta} = \dfrac{U_{ab} - R(i_a - i_b) - L\dfrac{d(i_a - i_b)}{dt}}{k_e\omega} \\ \dfrac{d(f_{bcr}(\theta))}{d\theta} = \dfrac{U_{bc} - R(i_b - i_c) - L\dfrac{d(i_b - i_c)}{dt}}{k_e\omega} \\ \dfrac{d(f_{car}(\theta))}{d\theta} = \dfrac{U_{ca} - R(i_c - i_a) - L\dfrac{d(i_c - i_a)}{dt}}{k_e\omega} \end{cases} \quad (2)$$

Function $H_{ij}(\theta)$ can be defined as follows:

$$H_{ij}(\theta) = \frac{d(f_{ijr}(\theta))}{d\theta} \quad (3)$$

Substituting Eq. (2) into Eq. (3) gives:

$$\begin{cases} H_{ab}(\theta) = \dfrac{d(f_{abr}(\theta))}{d\theta} = \dfrac{U_{ab} - R(i_a - i_b) - L\dfrac{d(i_a - i_b)}{dt}}{k_e\omega} \\ H_{bc}(\theta) = \dfrac{d(f_{bcr}(\theta))}{d\theta} = \dfrac{U_{bc} - R(i_b - i_c) - L\dfrac{d(i_b - i_c)}{dt}}{k_e\omega} \\ H_{ca}(\theta) = \dfrac{d(f_{car}(\theta))}{d\theta} = \dfrac{U_{ca} - R(i_c - i_a) - L\dfrac{d(i_c - i_a)}{dt}}{k_e\omega} \end{cases} \quad (4)$$

Function $G_i(\theta)$ can be defined as:

$$\begin{cases} G_x(\theta) = \dfrac{H_{ab}(\theta)}{H_{ca}(\theta)} = \dfrac{U_{ab} - R(i_a - i_b) - L\dfrac{d(i_a - i_b)}{dt}}{U_{ca} - R(i_c - i_a) - L\dfrac{d(i_c - i_a)}{dt}} \\ G_y(\theta) = \dfrac{H_{ca}(\theta)}{H_{bc}(\theta)} = \dfrac{U_{ca} - R(i_c - i_a) - L\dfrac{d(i_c - i_a)}{dt}}{U_{bc} - R(i_b - i_c) - L\dfrac{d(i_b - i_c)}{dt}} \\ G_z(\theta) = \dfrac{H_{bc}(\theta)}{H_{ab}(\theta)} = \dfrac{U_{bc} - R(i_b - i_c) - L\dfrac{d(i_b - i_c)}{dt}}{U_{ab} - R(i_a - i_b) - L\dfrac{d(i_a - i_b)}{dt}} \end{cases} \quad (5)$$

The function $H_{ij}(\theta)$, $G_i(\theta)$, phase current and commutation signal are shown in Fig. 3.

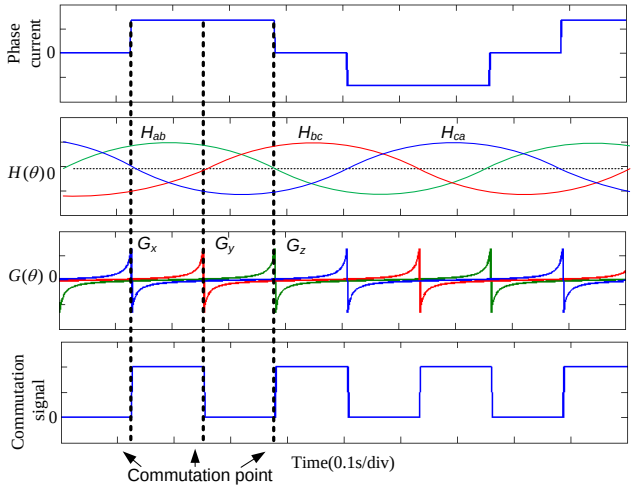

Fig. 3. Function $H_{ij}(\theta)$, $G_i(\theta)$, phase current and commutation signal.

As shown in Eq. (5), the $G_i(\theta)$ function is a speed–independent flux linkage function. The zero–crossing point of $H_{ij}(\theta)$ is corresponding to the extreme point of $G_i(\theta)$ function and the commutation point from Fig. 3. Theoretically, the $G_i(\theta)$ function can be used to estimate the rotor position from near zero to high speed.

III. The Optimized G Function and the Analyses of the Motor Terminal Voltage

A. *The influence of rotor position detection based on G function*

In practice, the detection accuracy of $G_i(\theta)$ function can be influenced by many factors, such as the interference and noise by high frequency PWM, diode freewheeling in heavy load conditions, calculation accuracy in the high speed range. The $G_i(\theta)$ function signal with the high frequency PWM and the diode freewheeling interference can be shown in Fig. 4

0885-8993 (c) 2017 IEEE. Personal use is permitted, but republication/redistribution requires IEEE permission. See http://www.ieee.org/publications_standards/publications/rights/index.html for more information.

This article has been accepted for publication in a future issue of this journal, but has not been fully edited. Content may change prior to final publication. Citation information: DOI 10.1109/TPEL.2017.2765355, IEEE Transactions on Power Electronics

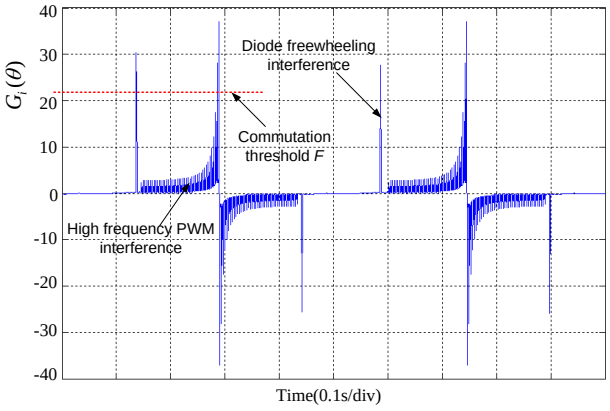

Fig. 4. The $G_i(\theta)$ function signal with high frequency PWM and diode freewheeling interference.

As the Fig. 4 shows, PWM for inverter brought the interference and the noise to $G_i(\theta)$ function. It is very difficult to extract the rotor position signal from the interference and the noise by high frequency PWM to reduce the estimation error. In order to solve this problem, the PAM is used to avoid the high frequency PWM interference. The inverter topology based on the buck converter and the PAM method for BLDC motor can be found in Fig. 1. The output frequency of the Inverter Bridge is equal to the rotor rotation frequency, and the buck converter is used to control the motor speed and current. The $G_i(\theta)$ function signal in PAM method can be shown in Fig. 5.

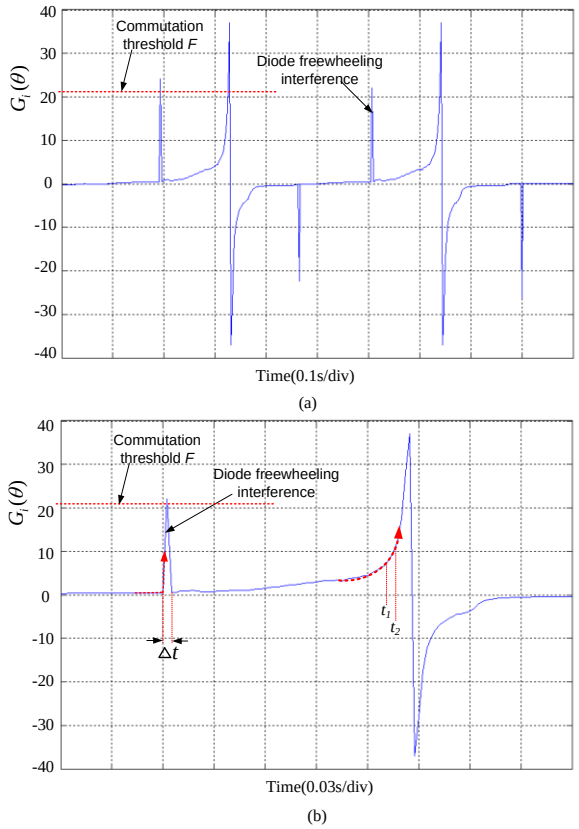

Fig. 5. The $G_i(\theta)$ function signal in PAM method. (a) The $G_i(\theta)$ function signal in PAM method with diode freewheeling interference. (b) The detail of diode freewheeling interference.

As the Fig. 5 shows, PAM method for the inverter avoided the high frequency PWM interference and noise. The influence of diode freewheeling interference is an approximate pulse, and the $G_i(\theta)$ function rose slowly from nearly zero to extreme point. In order to filter out the diode freewheeling interference, we analyzed the change rate of commutation threshold under different circumstances in detail. In order to increase the universality of the proposed method, we supposed that the duration of the diode freewheeling interference is Δt, the rotation period (t_r) should be greater than $10 \cdot \Delta t$, and the speed of the BLDC motor can be expressed as:

$$n_r = \frac{60}{p} \cdot \frac{1}{t_r} \le \frac{600}{p} \cdot \frac{1}{\Delta t} \tag{6}$$

As the interference value is pulse peak, the sampling of the commutation threshold F can be set once every Δt_G s, the detail of diode freewheeling interference and the extreme point of $G_i(\theta)$ can be shown in Fig. 6.

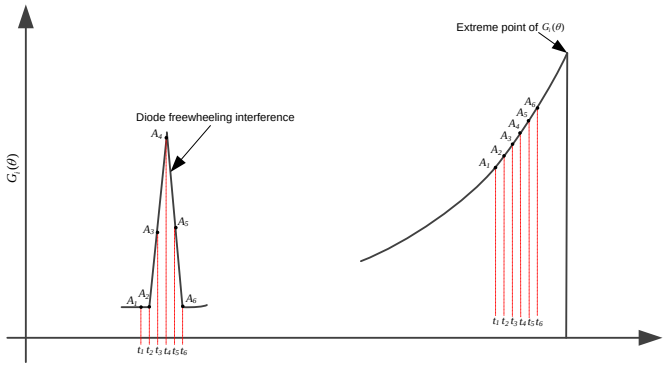

Fig. 6. The detail of diode freewheeling interference and the extreme point of $G_i(\theta)$.

The change rate of commutation threshold can be expressed as:

$$\Delta G_x(t_1) = \left| \frac{G_x(t_i) - G_x(t_{i-1})}{t_i - t_{i-1}} \right| = \left| \frac{A_i - A_{i-1}}{\Delta t_G} \right| \tag{7}$$

The change rate of commutation threshold is very different under the diode freewheeling interference and the normal $G_i(\theta)$ function. The relationship between them can be expressed as:

$$\Delta G_x(t_D) \ge \Delta G_x(t_F) \ge \Delta G_x(t_N) \tag{8}$$

where $\Delta G_x(t_D)$ is the change rate of commutation threshold under the diode freewheeling interference, $\Delta G_x(t_N)$ is the change rate of commutation threshold under the normal $G_i(\theta)$ function, and $\Delta G_x(t_F)$ is the change rate of commutation threshold to distinguish them. $\Delta G_x(t_F)$ was influenced by three factors: sampling time Δt_G, load torque and motor speed. As the interference value is pulse peak, we suppose that the diode freewheeling interference is symmetrical. When the sampling time $\Delta t_G \le \frac{1}{5} \cdot \Delta t$, the diode freewheeling interference can be detected wherever the sampling points are. The software algorithm need to judge the change rate of commutation threshold is the diode freewheeling interference

0885-8993 (c) 2017 IEEE. Personal use is permitted, but republication/redistribution requires IEEE permission. See http://www.ieee.org/publications_standards/publications/rights/index.html for more information.

This article has been accepted for publication in a future issue of this journal, but has not been fully edited. Content may change prior to final publication. Citation information: DOI 10.1109/TPEL.2017.2765355, IEEE Transactions on Power Electronics

or the normal $G_i(\theta)$ function. Therefore, the commutation error angle caused by software filter can be expressed as:

$$\psi_s = \frac{2\pi \cdot \Delta t_G}{t_r} \le \frac{2\pi \cdot \Delta t_G}{10 \cdot \Delta t} \le \frac{2\pi \cdot \Delta t}{5 \times 10 \cdot \Delta t} = \frac{\pi}{25} \tag{9}$$

As the three-phase six-state control strategy is used to drive the BLDC motor, the commutation error angle ($\frac{\pi}{25}$) cannot cause the motor lose step.

Based on the above analysis, the relationship between the motor speed and the duration of the diode freewheeling interference can be obtained by Eq. (6), and the software filter can be designed by Eq. (6), (7), (8). The diode freewheeling interference can be filtered out by software filter, and the commutation error angle can be compensated by Eq. (29). In this paper, $\Delta t_G = 0.001$, the rated speed of the BLDC motor is 1000 rpm, and the rotation period is about 0.06 s, the diode freewheeling interference (Δt) is about 0.005, and $\Delta G_x(t_F) = 3000$. The Δt and $\Delta G_x(t_F)$ are got by many simulation and experimental results.

The commutation signal can be got from the commutation threshold F, when the value of $G_i(\theta)$ function is greater than the commutation threshold F_s (the best commutation threshold, it can be obtained by many experimental results), the motor start to commutation. The maximum commutation error angle caused by the software filter can reach to 1.2 degrees in this paper. The estimation of $G_i(\theta)$ function signal is influenced by the motor parameters. And the off–line motor parameters will be changed after long-time operation. In order to solve the problem of the calculation accuracy in the high speed range, the Eq. (5) can be simplified as follow:

$$G_x(\theta) = \frac{H_{ab}(\theta)}{H_{ca}(\theta)} = \frac{U_{ab} - R(i_a - i_b) - L\dfrac{d(i_a - i_b)}{dt}}{U_{ca} - R(i_c - i_a) - L\dfrac{d(i_c - i_a)}{dt}} \approx \frac{U_{ab}}{U_{ca}} \tag{10}$$

From Eq. (5) and Eq. (10), the simplified error can be shown as follow:

$$\begin{aligned}\Delta G(\theta) = G_x(\theta) - G_x(\theta) &= \frac{U_{ab} - R(i_a - i_b) - L\dfrac{d(i_a - i_b)}{dt}}{U_{ca} - R(i_c - i_a) - L\dfrac{d(i_c - i_a)}{dt}} - \frac{U_{ab}}{U_{ca}} \\ &= \frac{RU_{ab}(i_c - i_a) - RU_{ca}(i_a - i_b) + LU_{ab}\dfrac{d(i_c - i_a)}{dt} - LU_{ca}\dfrac{d(i_a - i_b)}{dt}}{U_{ca}\left[U_{ca} - R(i_c - i_a) - L\dfrac{d(i_c - i_a)}{dt}\right]} \approx 0\end{aligned} \tag{11}$$

As shown in Eq. (11), the resistance and the inductance are very small and the commutation time is very short. The simplified $\tilde{G_i}(\theta)$ has little influence in the amplitude and the phase angle. Therefore, the simplified $\tilde{G_i}(\theta)$ can be used to estimate the commutation point.

Owing to the three–phase six–state control strategy of the BLDC motor, the commutation signal was obtained from the zero–crossing points of back–EMF. For the method based on $G_i(\theta)$ function, the commutation signal got from the extreme point of $G_i(\theta)$ function. Based on analysis mentioned above, the $e_{ca} = e_c - e_a = 0$ corresponded to the extreme point of $G_i(\theta)$ function. The line–to–line back–EMFs can be expressed as:

$$e_{ca} = e_c - e_a = (U_c - U_a) - R(i_c - i_a) - L\frac{d(i_c - i_a)}{dt} \tag{12}$$

Because the PAM technique is used in this paper, the zero–crossing points of line–to–line back–EMFs can be replaced by the zero–crossing points of line–to–line voltages. At this time, $U_{ca} = U_c - U_a = 0$. In the motor start–up stage, for a balanced wye–connected BLDC motor, the three–phase currents can be expressed as:

$$i_a + i_b + i_c = 0 \tag{13}$$

Suppose the current flow from T_3 to T_2, $i_b = -i_c$, $i_a = 0$, the electromagnetic torque can be expressed as:

$$T_e = \frac{e_b i_b + e_c i_{bc}}{\Omega} \tag{14}$$

In order to achieve the minimum torque ripple, the bus voltage $U_d = 4E$, where E is the amplitude of phase back–EMF. When the impedance voltage drop is neglected, the phase voltage, phase current and commutation error can be shown in Fig. 7.

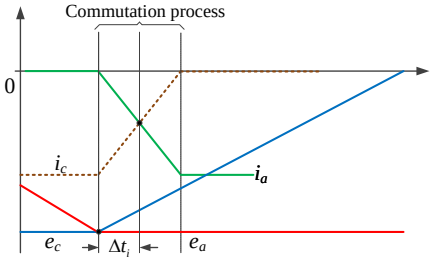

Fig. 7. The waveforms of the phase voltage, phase current and commutation error.

As shown in Fig. 7, the commutation error is Δt_i. The Δt_i is relate to the motor speed. The commutation process time can be expressed as:

$$t_i \approx 2\Delta t_i = \frac{6LI}{U_d + 2E} \tag{15}$$

where I is the amplitude of the phase current, and in this paper the commutation error $\Delta t_{i\max} \approx 0.05$ (In the low speed range, L=0.075 mH, $U_d \ge 100$, $I \le 12$, $E \approx 10$). The commutation error angle $\Delta\varepsilon_{i\max} \le 18$ (when the motor speed is lower than 30 rpm). Therefore, the maximum commutation error is in the "three–step startup stage". And the commutation error reduced with the increase of the motor speed. However, the temperature drift of the detection circuit parameter and the cumulative error in the calculation caused the commutation error. It is very necessary to analyze the change of the motor terminal voltage in the commutation process.

B. The influence of motor commutation error on the motor terminal voltage

The motor phase back–EMFs in one cycle can be

0885-8993 (c) 2017 IEEE. Personal use is permitted, but republication/redistribution requires IEEE permission. See http://www.ieee.org/publications_standards/publications/rights/index.html for more information.

This article has been accepted for publication in a future issue of this journal, but has not been fully edited. Content may change prior to final publication. Citation information: DOI 10.1109/TPEL.2017.2765355, IEEE Transactions on Power Electronics

approximately expressed as:

$$e_b=\begin{cases}\dfrac{6}{\pi}K_e\omega^2 t & 0\le\omega t\le\dfrac{\pi}{6}\\ K_e\omega & \dfrac{\pi}{6}\le\omega t\le\dfrac{5\pi}{6}\\ -\dfrac{6}{\pi}K_e\omega^2 t+6K_e\omega & \dfrac{5\pi}{6}\le\omega t\le\dfrac{7\pi}{6}\\ -K_e\omega & \dfrac{7\pi}{6}\le\omega t\le\dfrac{11\pi}{6}\\ \dfrac{6}{\pi}K_e\omega^2 t-12K_e\omega & \dfrac{11\pi}{6}\le\omega t\le 2\pi\end{cases}\tag{16}$$

where K_e is the coefficient of the phase back–EMF, ω is the motor angular velocity. Taking the phase B as an example, the voltage of neutral point from Eq. (1) can be given as:

$$U_N=\frac{U_{d2}}{2}\tag{17}$$

When the commutation is accurate, the B phase voltage can be given as follow:

$$U_{b1}=U_N+e_b\tag{18}$$

When $\omega t=\dfrac{\pi}{6}$, the phase back–EMF can be given as:

$$e_b=\frac{6}{\pi}K_e\omega^2 t\tag{19}$$

Substituting Eq. (19) into Eq. (18) gives:

$$U_{b1}=U_N+\frac{6}{\pi}K_e\omega^2 t\tag{20}$$

When $\omega t=\dfrac{5\pi}{6}$, the phase back–EMF can be given as:

$$e_b=K_e\omega\tag{21}$$

Substituting Eq. (21) into Eq. (18) gives:

$$U_{b1}=U_N+K_e\omega\tag{22}$$

Because the commutation time interval is very short in a commutation period, it can be regarded as constant for the BLDC motor. When the commutation is accurate, the integral area of phase voltage can be expressed as:

$$S_1=\int_0^{\frac{\pi}{6}}U_{b1}=\int_0^{\frac{\pi}{6}}\left(U_N-\frac{6}{\pi}K_e\omega^2 t\right)dt\tag{23}$$

$$S_2=\int_{\frac{5\pi}{6}}^{\pi}U_{b2}=\int_{\frac{5\pi}{6}}^{\pi}\left(U_N+K_e\omega\right)dt\tag{24}$$

When $\Delta S=S_1-S_2=0$, the commutation is accurate, the integral area of the phase voltage is equal as the Fig. 8 shows.

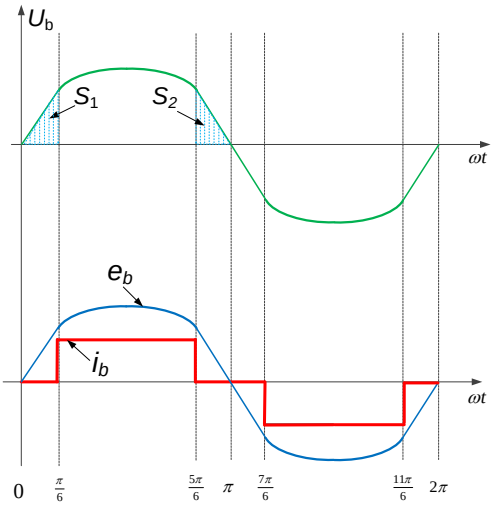

Fig. 8. When commutation is accurate, the waveform of phase voltage, phase Back–EMF and phase current.

If the commutation is not accurate, the integral area of phase voltage will appear deviation. When the commutation is advanced, $\omega t=\dfrac{\pi}{6}-\Delta\theta$, $\Delta\theta$ is the advanced angle. At this time, the B phase voltage can be given as:

$$U_{b1}<U_N-\frac{6}{\pi}K_e\omega^2 t\tag{25}$$

When B phase turn off, $\omega t=\dfrac{5\pi}{6}-\Delta\theta$, at this time, the B phase voltage can be given as:

$$U_{b1}>U_N+K_e\omega\tag{26}$$

Similarly, from Eq. (23), (24), (25) and (26), the integral area of phase voltage can be given as:

$$\Delta S=S_1-S_2<\int_0^{\frac{\pi}{6}}\left(U_N-\frac{6}{\pi}K_e\omega^2 t\right)dt-\int_{\frac{5\pi}{6}}^{\pi}\left(U_N+K_e\omega\right)dt=0\tag{27}$$

Similarly, when the commutation is lagged, the integral area of phase voltage can be given as:

$$\Delta S=S_1-S_2>\int_0^{\frac{\pi}{6}}\left(U_N-\frac{6}{\pi}K_e\omega^2 t\right)dt-\int_{\frac{5\pi}{6}}^{\pi}\left(U_N+K_e\omega\right)dt=0\tag{28}$$

Whenever the commutation is advanced or lagged, the integral area of the phase voltage is not equal. The waveforms of the phase voltage, the phase back–EMF and the phase current can be shown in Fig. 9.

As the Fig. 9 shows, when the commutation is not accurate, the phase voltage appeared deviation, the integral area of phase voltage is not equal and the current peak value is increased. With the increase of commutation error, the efficiency of the system is reduced, the motor may lose step or be locked.

0885-8993 (c) 2017 IEEE. Personal use is permitted, but republication/redistribution requires IEEE permission. See http://www.ieee.org/publications_standards/publications/rights/index.html for more information.

This article has been accepted for publication in a future issue of this journal, but has not been fully edited. Content may change prior to final publication. Citation information: DOI 10.1109/TPEL.2017.2765355, IEEE Transactions on Power Electronics

IV. A Novel Sensorless Closed–Loop Control System for BLDC Motor

Based on the analysis mentioned above, a novel sensorless closed–loop commutation error adaptive correction strategy has been present, as shown in Fig. 10.

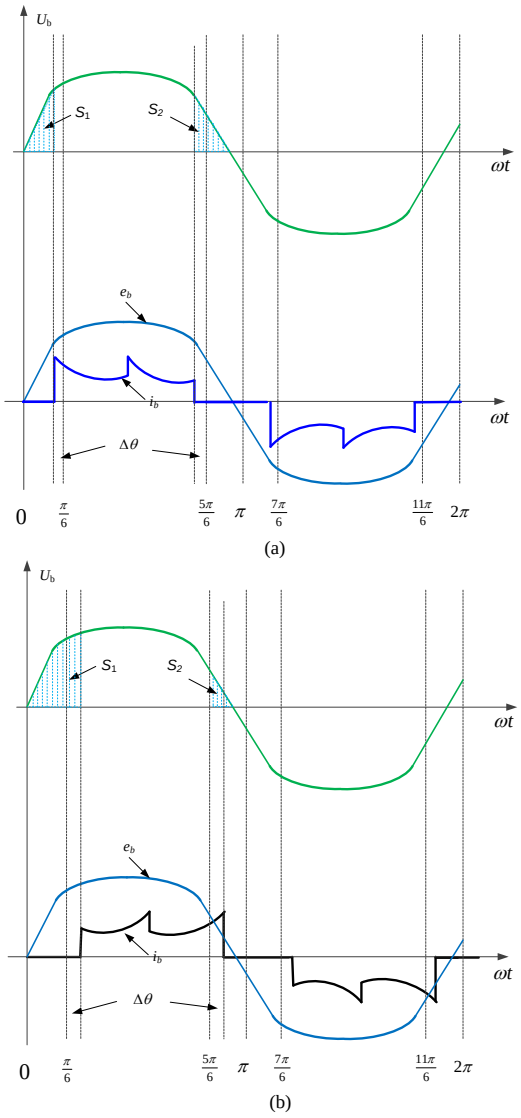

Fig. 9. When commutation is not accurate, the waveform of phase voltage, phase back–EMF and phase current. (a) When the commutation is advanced. (b) When the commutation is lagged.

As the Fig. 10 shows, the control system block diagram contains the speed closed–loop and the current closed–loop. The speed controller is used to respond the external disturbance. The torque can be rapidly compensated by adjusting the current controller. The motor speed can be calculated by the phase voltage zero–crossing point, and the $G_i^{\sim}(\theta)$ can be calculated by Eq. (7) from line–to–line voltages detection. The integral area of the phase voltage can be calculated by Eq. (23) and (24). In actual operation, the integral area of the line–to–line voltages can also express the commutation error. Therefore, ΔS is got from the line–to–line voltages, the commutation threshold F can be expressed as follow:

$$F_{(\omega t)} = G_{i\,(\omega t)}^{\sim} \pm \left|K_p \Delta S\right| \pm \left|K_I \int_0^t \Delta S dt\right| \tag{29}$$

The sign is determined by the integral area deviation (ΔS) of the phase voltage, it can be described as:

$$sign(\Delta S) = \begin{cases} +1 & \Delta S < 0 \\ -1 & \Delta S > 0 \end{cases} \tag{30}$$

In fact, it is not a negative proportional gain in the PI regulator, but an opposite in sign with ΔS . The best commutation point can be decided by the commutation threshold F, which is calculated by $G_i^{\sim}(\theta)$. The minor adjustment is achieved by the correction quantity ($\left|K_p \Delta S\right| \pm \left|K_I \int_0^t \Delta S dt\right|$). When the commutation is advanced, $\Delta S < 0$, F is increased by Eq. (29).

When the commutation is lagged, $\Delta S > 0$, F is reduced by Eq. (29), until $\Delta S = 0$. The "Threshold F and commutation logic" block has two functions of the commutation and the commutation error compensation. The commutation signal was got from the zero crossing of phase voltage, which completes the three–phase six–state control strategy for the BLDC motor. The commutation error compensation was got from Eq. (11) ($G_x(\theta) \approx \frac{U_{ab}}{U_{ca}}$), Eq. (29) ($F_{(\omega t)} = G_{i\,(\omega t)}^{\sim} \pm \left|K_p \Delta S\right| \pm \left|K_I \int_0^t \Delta S dt\right|$) and the motor speed. F increased with the increase of the motor speed. The relationship between F and the motor speed can be shown in Fig. 11.

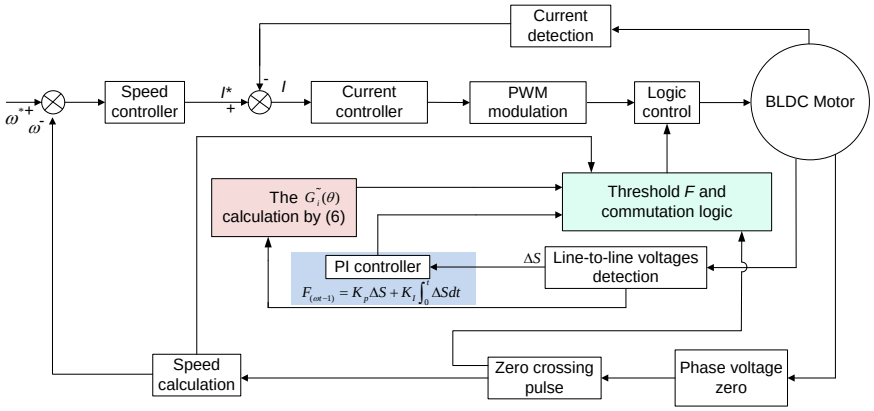

Fig. 10. The novel sensorless closed–loop commutation error adaptive correction block diagram.

0885-8993 (c) 2017 IEEE. Personal use is permitted, but republication/redistribution requires IEEE permission. See http://www.ieee.org/publications_standards/publications/rights/index.html for more information.

This article has been accepted for publication in a future issue of this journal, but has not been fully edited. Content may change prior to final publication. Citation information: DOI 10.1109/TPEL.2017.2765355, IEEE Transactions on Power Electronics

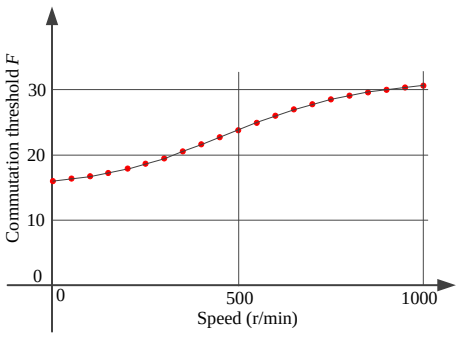

Fig. 11. The relationship between commutation threshold F and the motor speed.

The relationship between F and the motor speed can be got from many experimental data. The different trapped objects have different F values. For the researched BLDC motor in this paper, many calculation and experiments have proved that $K_p = 7.25$ and K_I =0.25 are the best parameters of the control system. The commutation error can be corrected rapidly and stability.

When the electromagnetic torque is greater than the load torque, the motor began to rotate. In order to ensure the success of the starting under unknown rotor information, two steps location strategy, which are the synthetic electromagnetic torque and the rotor position by two steps location strategy, were used as shown in Fig. 12.

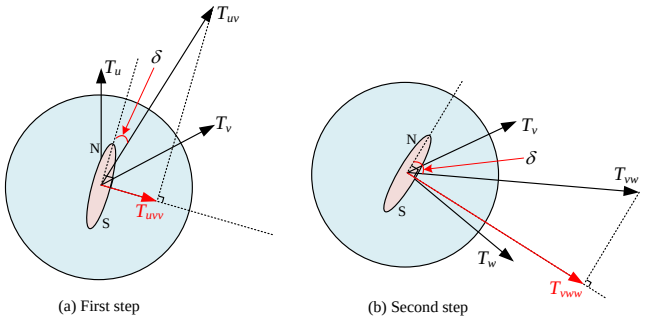

(a) First step (b) Second step

Fig. 12. The synthetic electromagnetic torque and rotor position by two steps location strategy.

The angle between the rotor position and the applied torque can be expressed as:

$$\delta = \sin^{-1}\frac{T_o}{I_s \cdot K_T} \tag{31}$$

where K_T is the torque coefficient, δ is the angle between the rotor position and the applied torque, T_o is the load torque. As shown in Fig. 12 (a), if δ is very small, a very large starting current is needed to rotate the rotor. When $\delta \approx 0$, the starting current $I_s \to +\infty$. Therefore, the two steps location method was proposed as shown in Fig. 12 (b). The constraint condition of the motor start–up stage is obtained as:

$$\begin{cases} I_s \le \dfrac{P_{\max}}{U_{\max}} \\ T_{es} \ge T_o \end{cases} \tag{32}$$

where $P_{\max}$ is the motor maximum power, $U_{\max}$ is the motor maximum voltage, T_{es} is the electromagnetic torque in the start–up stage. The maximum starting current is given as:

$$I_s = \frac{T_o}{K_T \sin\delta_{\lim}} \tag{33}$$

where $\delta_{\lim}$ is the minimum angle between the rotor position and the applied torque. The starting current can be limited by PWM method as Eq. (32) illustrated. The starting current determines whether the rotor can be dragged and whether the rotor can rotate to the certain location by location time. In a commutation period, the average electromagnetic torque can be given as:

$$T_{avg} = \frac{1}{2\rho}\int_{-\rho}^{\rho} K_T I_s d\theta \tag{34}$$

where ρ is the rotor rotation angle, the time of the rotor from stationary position to the certain position can be given as:

$$T_t = \sqrt{\frac{2\rho}{\alpha}} \tag{35}$$

where $\alpha = \dfrac{T_{avg}}{J}$ is the rotor average angular acceleration, J is the rotor inertia. The Eq. (35) can be simplified as:

$$T_t = \sqrt{\frac{2\rho J}{T_{avg}}} = \sqrt{\frac{4\rho^2 J}{\int_{-\rho}^{\rho} K_T I_s d\theta}} \tag{36}$$

The location time can be calculated by Eq. (36) according to the motor parameters. The terminal voltage and the rotational frequency are needed to increase in the external synchronization stage.

V. Experimental Results

A. Experiment Platform Setup

The proposed novel sensorless closed–loop commutation error adaptive correction strategy has been implemented on a BLDC motor for petroleum drilling system. The experimental platform is shown in Fig. 13, and the detailed parameters of the system device controller are listed in Table I. The experimental parameters of the BLDC motor are listed in Table II.

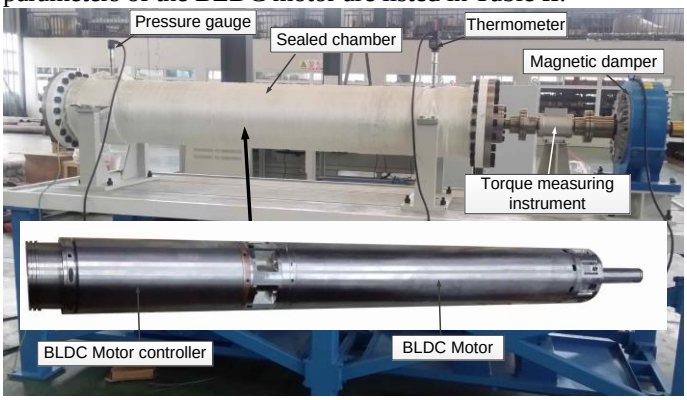

Fig. 13. The experimental platform is consisted of control system and experimental motors.

0885-8993 (c) 2017 IEEE. Personal use is permitted, but republication/redistribution requires IEEE permission. See http://www.ieee.org/publications_standards/publications/rights/index.html for more information.

This article has been accepted for publication in a future issue of this journal, but has not been fully edited. Content may change prior to final publication. Citation information: DOI 10.1109/TPEL.2017.2765355, IEEE Transactions on Power Electronics

In order to simulate the underground working environment of the petroleum drilling system, the experimental platform has been built as Fig. 13 shows. Put the BLDC motor in a sealed chamber. The sealed chamber was fully filled with oil. The pressure of the sealed chamber can reach to about 1.10×10^{7} Pa, and the temperature can reach to about 90℃. The magnetic damper was used to simulate the load torque, and it can be detected by the torque measuring instrument.

TABLE I SYSTEM DEVICE DETAILS

Parameter	Value
Digital controller	DSP (TMS320F28335)
Clock frequency	40 MHz
Inverter Bridge	SKM 50GB123D
Inverter Bridge driver	Concept 2SD315A
Power Supply	MIWE S－500－24

Table II PARAMETERS OF THE MOTOR USED IN THE EXPERIMENT

Surface Mounted BLDC Motor	
Rated DC voltage	1000 V
Rated current	12 A
Rated speed, *n*	1000 rpm
Rated Power	12 kW
Number of pole pairs, *P*	4
Rated torque, *T*	200 N.m
Back–EMF constant, K_e	0.385 V/ rpm
Phase resistance, *R*	1.2 Ω
Phase inductance, *L*	75 mH

The corresponding relation between $\tilde{G_i}(\theta)$ function and the commutation table is shown in Table III.

Table III THE CORRESPONDING RELATION OF $\tilde{G_i}(\theta)$ FUNCTION AND COMMUTATION TABLE

Mode	$\tilde{G_i}(\theta)$ Function	Commutation device
Mode 1 and Mode 4	$G_x(\theta)=\frac{U_{ab}}{U_{ca}}$	T3+, T2－ or T3+, T4－
Mode 2 and Mode 5	$G_y(\theta)=\frac{U_{ca}}{U_{bc}}$	T5+, T4－ or T5+, T6－
Mode 3 and Mode 6	$G_z(\theta)=\frac{U_{bc}}{U_{ab}}$	T1+, T6－ or T1+, T2－

B. *Experiment 1–start–up*

The “three step” start–up control strategy was used both in the traditional sensorless start–up and the proposed sensorless control strategy for the BLDC motor [35]. If the sensorless control strategy is based on the back–EMF, the speed of motor will be needed to rise until the rotor position can be detected by the detection circuit according to the back–EMF signal. The $\tilde{G_i}(\theta)$ function can detect the rotor position by the speed–independent flux linkage function, and the rotor position signal can be detected in the low speed range, as shown in Fig. 14.

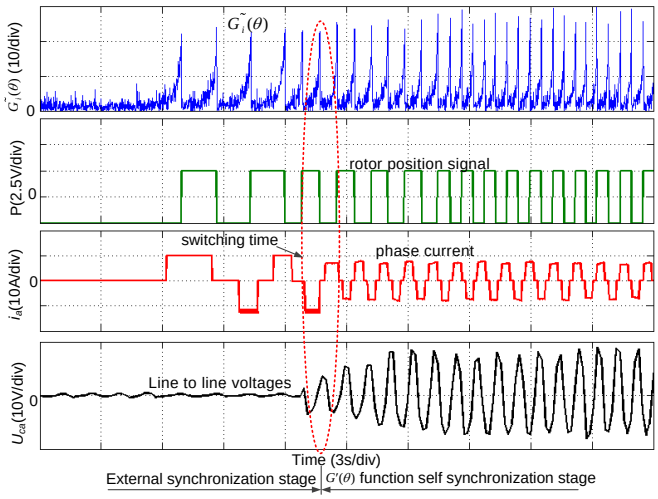

Fig. 14. The waveforms of $\tilde{G_i}(\theta)$ Function, rotor position signal, phase current and line to line voltages in start–up stage.

As the Fig. 14 shows, the $\tilde{G_i}(\theta)$ function can be detected until the speed reached to 30 rpm, and then the control strategy began to switch from the external–synchronization stage to the self–synchronization stage. The commutation point can be estimated by $\tilde{G_i}(\theta)$ function and the commutation error can be ignored in the low speed range. The duration time of the start–up stage was about 7 s. Fig. 15 shows the line–to–line voltages, phase current and the rotor position signal when the sensorless control strategy was based on the back–EMF.

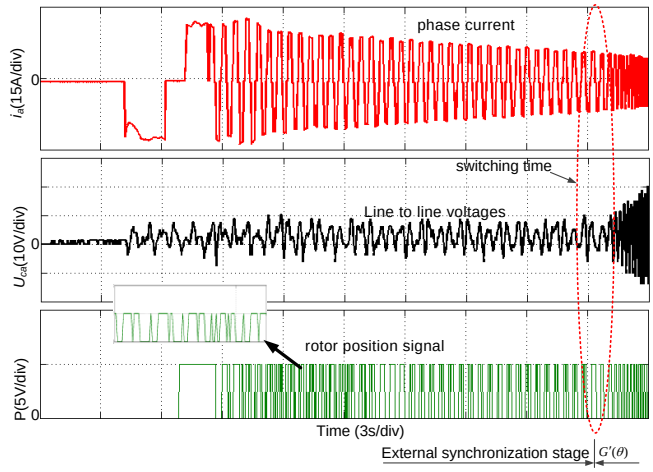

Fig. 15. The waveforms of phase current, line–to–line voltages and rotor position signal based on back–EMF sensorless control strategy in start–up stage.

As shown in Fig. 15, when the sensorless control strategy was based on the back–EMF, the rotor position signal cannot be detected until the speed reached to 100 rpm, the duration time of the start–up stage is about 25 s. The design of the start–up curve based on the back–EMF sensorless control strategy was very complex. Fig. 16 shows the line–to–line voltages, phase current and the hall sensor signal when the start–up control strategy was based on hall sensor.

0885-8993 (c) 2017 IEEE. Personal use is permitted, but republication/redistribution requires IEEE permission. See http://www.ieee.org/publications_standards/publications/rights/index.html for more information.

This article has been accepted for publication in a future issue of this journal, but has not been fully edited. Content may change prior to final publication. Citation information: DOI 10.1109/TPEL.2017.2765355, IEEE Transactions on Power Electronics

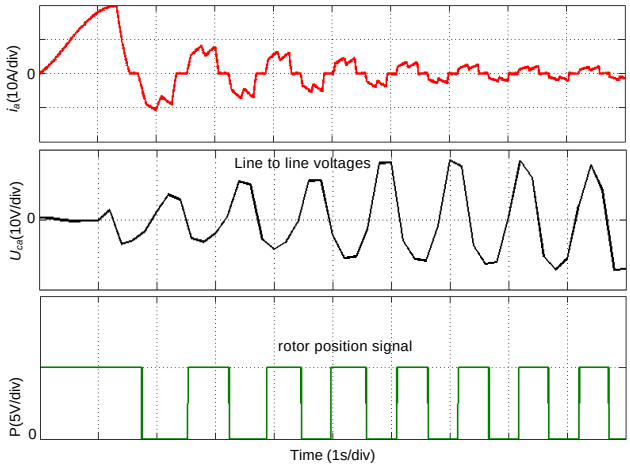

Fig. 16. The waveforms of phase current, line–to–line voltages and rotor position signal based on hall sensor in start - up stage.

As shown in Fig. 16, the start-up process is very smooth based on hall sensor. The rotor position can be detected at about 20 rpm. From Fig. 14, Fig. 15 and Fig. 16, it can be seen that the effect based on $G_i^{\sim}(\theta)$ function control strategy is better than the back–EMF sensorless control strategy.

C. *Experiment 2 – high speed*

In the high speed range, the commutation accuracy is based on the installation accuracy of hall sensor when the commutation signals were collected by the hall sensor. The phase current, line–to–line voltages and the rotor position are shown in Fig. 17 at the speed of 500 rpm and 1000 rpm.

Fig. 17 (a) shows the waveforms of the phase current, the line–to–line voltages and the rotor position signal at the speed of 500 rpm when the installation of hall sensor is advanced. The phase current and the line–to–line voltages became distorted, and the integral area of the line–to–line voltages was not equal. When the commutation is advanced, $\Delta S < 0$, this is consistent with the theoretical analysis. Fig. 17 (b) shows the waveforms of phase current, the line–to–line voltages and the rotor position signal at the speed of 500 rpm when the installation of hall sensor is lagged. The integral area of the line–to–line voltages was not equal and $\Delta S > 0$, this is consistent with the theoretical analysis too. So the similar conclusions at the speed of 1000 rpm can be concluded as Fig. 17 (c) and Fig. 17 (d) show.

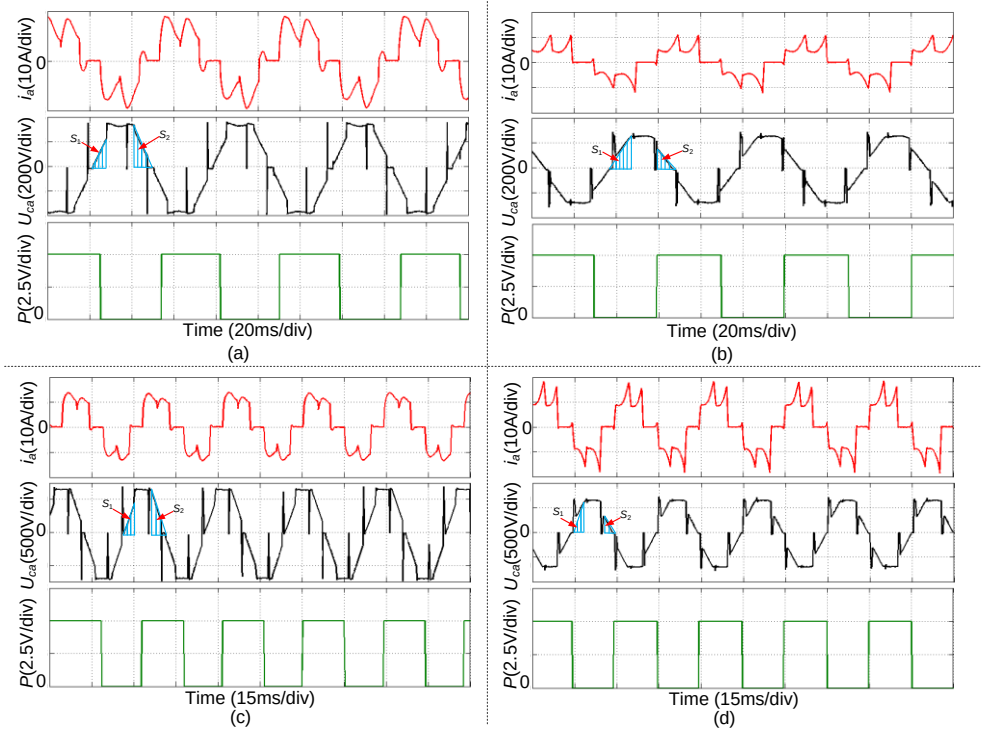

Fig. 17. The waveforms of phase current, line–to–line voltages and rotor position signal based on hall sensor. (a) The installation advanced at the speed of 500 rpm. (b) The installation lagged at the speed of 500 rpm. (c) The installation advanced at the speed of 1000 rpm. (d) The installation lagged at the speed of 1000 rpm.

When using the sensorless control strategy based on the back–EMF, the detection of the commutation point would be delayed by the low pass filter circuit and the software algorithm. The commutation error is accumulated with the increase of the motor speed. The waveforms of phase current, line–to–line voltages and rotor position signal based on back–EMF are shown in Fig. 18.

As shown in Fig. 18 (a), the commutation was lagged by the low pass filter of the detection circuit. And the lagged angle increased with the motor speed increase. When the lagged angle was more than 30 electric degrees, he motor will need to switch the commutation mode or it will be locked. The similar conclusions are shown in Fig. 18 (b). The commutation point can be estimated by $G_i^{\sim}(\theta)$ function. The integral area of the line–to–line voltages was used to correct the commutation error. The waveforms of the phase current, the line–to–line voltages and $G_i^{\sim}(\theta)$ function signal at the speed of 1000 rpm are shown

0885-8993 (c) 2017 IEEE. Personal use is permitted, but republication/redistribution requires IEEE permission. See http://www.ieee.org/publications_standards/publications/rights/index.html for more information.

This article has been accepted for publication in a future issue of this journal, but has not been fully edited. Content may change prior to final publication. Citation information: DOI 10.1109/TPEL.2017.2765355, IEEE Transactions on Power Electronics

in Fig. 19.

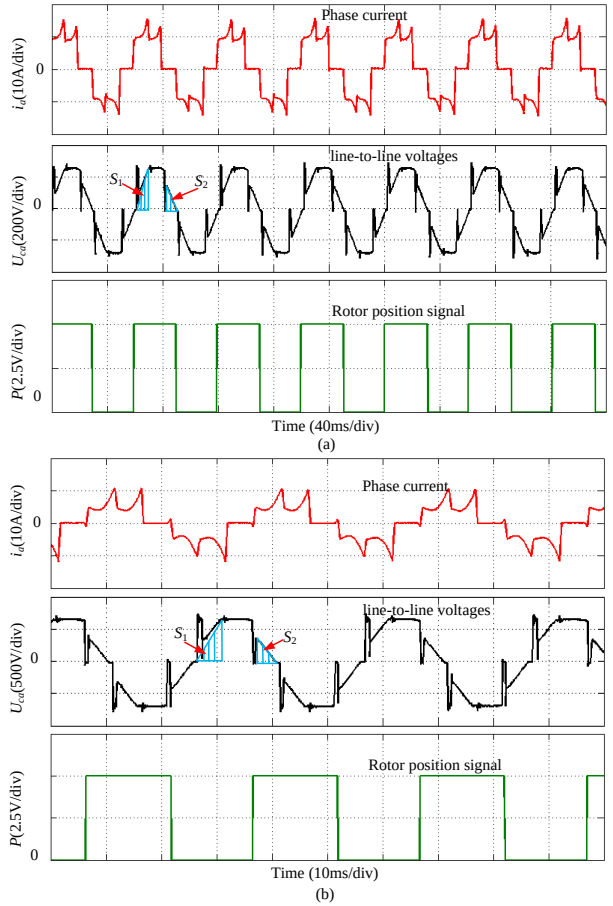

Fig. 18. The waveforms of phase current, line–to–line voltages and rotor position signal based on back–EMF sensorless control strategy. (a) The commutation is lagged about 3 electric degrees at the speed of 500 rpm. (b) The commutation is lagged about 5 electric degrees at the speed of 1000 rpm.

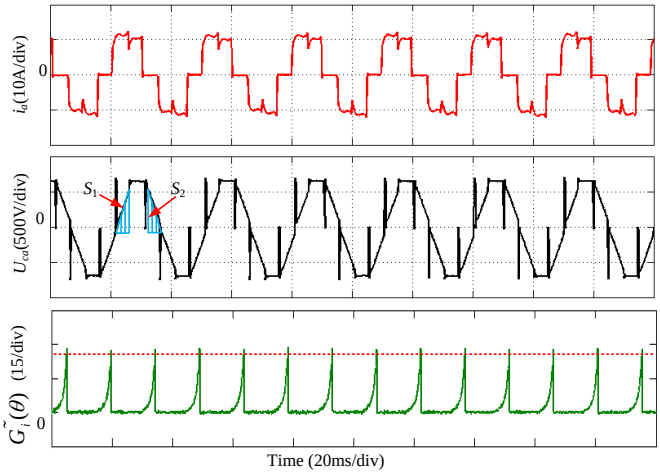

Fig. 19. The waveforms of phase current, line–to–line voltages and $\tilde{G}_i(\theta)$ function signal based on the novel sensorless control strategy proposed in this paper.

As shown in Fig. 19, the commutation error can be corrected by the novel sensorless control strategy proposed in this paper. The phase current was symmetrical perfectly, and the integral area of the line–to–line voltages was equal. The diode freewheeling interference can be filtered by a soft filter as Eq. (6) illustrated. At that time, $\Delta S = 0$, the commutation threshold F remain constant.

When the motor speed increased or decreased, the experimental results including the detected $\tilde{G}_i(\theta)$ function waveform can be shown in Fig. 20.

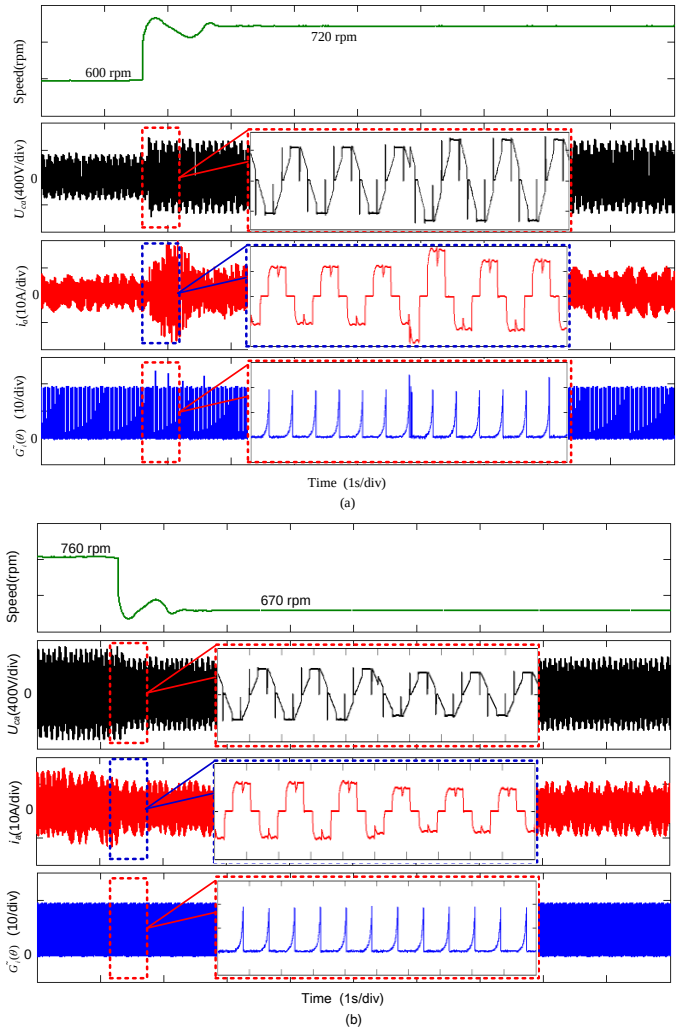

Fig. 20. When the motor speed is increased/decreased, the waveforms of experimental results; (a) When the motor speed is increased; (b) When the motor speed is decreased.

As shown in Fig. 20, when the motor speed increased or decreased, the phase current and the line–to–line voltages have disturbance in a short time. The disturbance can be corrected by the control strategy (Eq. (11)). Therefore, the novel sensorless control strategy has the velocity perturbation ability, which reflects its potential value for the industrial application. When the load torque increased, this sensorless control strategy has a certain ability to resist disturbance. The anti–interference experiment results can be shown in Fig. 21.

0885-8993 (c) 2017 IEEE. Personal use is permitted, but republication/redistribution requires IEEE permission. See http://www.ieee.org/publications_standards/publications/rights/index.html for more information.

This article has been accepted for publication in a future issue of this journal, but has not been fully edited. Content may change prior to final publication. Citation information: DOI 10.1109/TPEL.2017.2765355, IEEE Transactions on Power Electronics

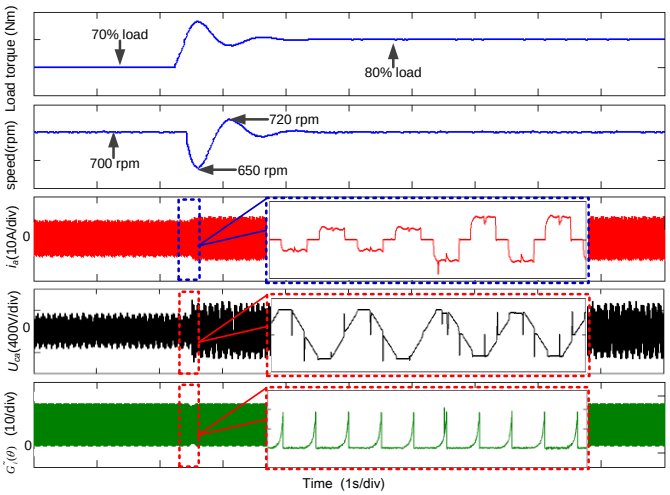

Fig. 21. The waveforms of phase current, line–to–line voltages and $G_i^{\sim}(\theta)$ function signal when the load torque is increased.

As shown in Fig. 21, when the load torque increased about 10 % of the rated torque, the phase current increase with the increase of the electromagnetic torque. In a short time, the BLDC motor speed is reduced, and the waveforms of the line–to–line voltages have small changes. The $G_i^{\sim}(\theta)$ function signal and the commutation point have little changes. Therefore, the novel sensorless control strategy proposed in this paper has the anti–disturbance ability, which reflects its potential value for the industrial application. The system efficiency was improved because of the accurate commutation. The comparison of the system efficiency between the accurate commutation and the error commutation is shown in Fig. 22.

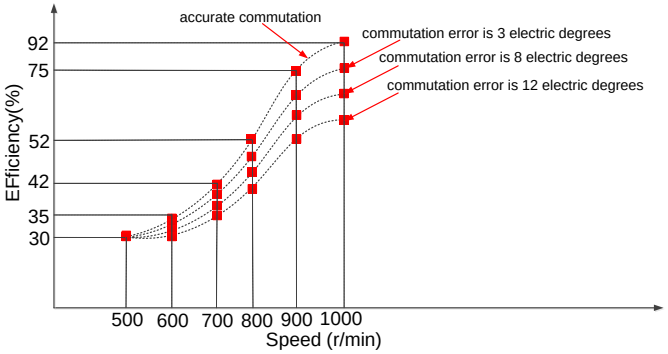

Fig. 22. The comparison of system efficiency between accurate commutation and error commutation.

As Fig. 22 shows, the system efficiency reduced because of the commutation error, and the system efficiency reduced with the increase of the commutation error angle.

VI. CONCLUSION

This paper proposed a novel adaptive compensation strategy of the position estimation commutation error for the sensorless BLDC motor drives. The compensation signal can be detected by a flux function, and the compensation error can be corrected by the deviation of the line–to–line voltages. Two key sensorless control strategy techniques of the BLDC motor have been resolved.

(a) Solve the starting problem. The $G_i^{\sim}(\theta)$ function control strategy can detect the rotor position at a very low speed, in this paper it is about 30 rpm (3% of rated speed). The software filter ensures that the rotor position signal can be detected from the interference and the noise by high frequency.

(b) Solve the problem of the compensation error in the high speed range. The compensation error can be corrected by the deviation of the line–to–line voltages. The system efficiency can be increased by the proposed commutation error correction strategy.

REFERENCES

[1] G. Liu, S. Chen, S. Zheng and X. Song. "Sensorless low–current start–up strategy of 100kW BLDC motor with small inductance". *IEEE Trans. Ind. Inform*., vol. 13, no. 3, pp. 1131–1140, Jun. 2017.

[2] S. Zheng, H. Li, B. Han, and J. Yang, "Power consumption reduction for magnetic bearing systems during torque output of control moment gyros," IEEE *Trans. Power Electron.*, vol. 32, no. 7, pp. 5752–5759, July. 2017.

[3] S. Zheng, B. Han, and L. Guo, "Composite hierarchical antidisturbance control for magnetic bearing system subject to multiple external disturbances," *IEEE Trans. Ind. Electron*., vol. 61, no. 12, pp. 7004–7012, Dec. 2014.

[4] J. Fang, S. Zheng, and B. Han, "AMB vibration control for structural resonance of double–gimbal control moment gyro with high–speed magnetically suspended rotor," *IEEE/ASME Trans. Mechatronics*, vol. 18, no. 1, pp. 32–43, Feb. 2013.

[5] X. Song, J. Fang, B. Han, and S. Zheng, "Adaptive Compensation Method for High-Speed Surface PMSM Sensorless Drives of EMF-Based Position Estimation Error," *IEEE Transactions on Power Electronics*, vol. 31, pp. 1438-1449, 2016..

[6] C. Hung, C. Lin, C. Liu, Jia–Yush Yen, "A variable–sampling controller for brushless DC motor drives with low–resolution position sensors," *IEEE Trans. Ind. Electron*., vol. 54, no. 5, pp. 2846–2852, Oct. 2007.

[7] X. Song, B. Han, S. Zheng, and J. Fang, "High-precision Sensorless Drive for High-speed BLDC Motors based on the Virtual 3rd harmonic back-EMF," *IEEE Transactions on Power Electronics*, to be published, doi: 10.1109/TPEL.2017.2688478.

[8] O. Scaglione, M. Markovic, and Y. Perriard, "First–pulse technique for brushless DC motor standstill position detection based on iron B–H hysteresis," *IEEE Trans. Ind. Electron*., vol. 59, no. 5, pp. 2319–2328, May. 2012.

[9] M. Carpaneto, P. Fazio, M. Marchesoni, and G. Parodi, "Dynamic performance evaluation of sensorless permanent–magnet synchronous motor drives with reduced current sensors," *IEEE Trans. Ind. Electron*., vol. 59, no. 12, pp. 4579–4589, Dec. 2012.

[10] W. Yuanyuan, D. Zhiquan, W. Xiaolin, L. Xing, and C. Xin, "Position sensorless control based on coordinate transformation for brushless DC motor drives," *IEEE Trans. Power Electron*., vol. 25, no. 9, pp. 2365–2371, Sept. 2010.

[11] X. Song, B. Han, S. Zheng, S. Chen, "A novel sensorless rotor position detection method for high-speed surface PM motors in a wide speed range". *IEEE Trans. Power Electron*., to be published, doi: 10.1109/TPEL.2017.2753289.

[12] L. Idkhajine, E. Monmasson, and A.Maalouf, "Fully FPGA–based sensorless control for synchronous AC drive using an extended Kalman filter," *IEEE Trans. Ind. Electron*., vol. 59, no. 10, pp. 3908–3918, Oct. 2012.

[13] J. Cai, Z. Deng, "Sensorless control of switched reluctance motor based on phase inductance vectors," *IEEE Trans. Power Electron*., vol. 27, no. 7, pp. 3410–3423, Jul. 2012.

[14] J. Shen and S. Iwasaki, "Sensorless control of ultrahigh–speed PM brushless motor using PLL and third harmonic back–EMF,"*IEEE Trans. Ind. Electron.*, vol. 53, no. 2, pp. 421 – 428, Apr. 2006.

[15] C. Xia, and X. Li, "Z–Source inverter–based approach to the zero–crossing point detection of back EMF for sensorless brushless DC motor," *IEEE Trans. Power Electron*., vol. 30, no. 3, pp.1488–1498, Mar. 2015.

[16] S. Chen, G. Liu, S. Zheng. "Sensorless control of BLDCM drives for a high–speed maglev blower using a low pass filter". *IEEE Trans. Power Electron*., vol. 32, no. 11, pp. 8845–8856, Nov. 2017.

0885-8993 (c) 2017 IEEE. Personal use is permitted, but republication/redistribution requires IEEE permission. See http://www.ieee.org/publications_standards/publications/rights/index.html for more information.

This article has been accepted for publication in a future issue of this journal, but has not been fully edited. Content may change prior to final publication. Citation information: DOI 10.1109/TPEL.2017.2765355, IEEE Transactions on Power Electronics

[17] N. Samoylenko, Q. Han, and J. Jatskevich, "Dynamic performance of brushless dc motors with unbalanced hall sensors," *IEEE Trans. Energy Convers*., vol. 23, no. 3, pp. 752–763, Sep. 2008.
[18] J. Shao, D. Nolan,M. Tsissier, and D. Swanson, "A novelmicrocontrollerbased sensorless brushless DC (BLDC) motor drive for automotive fuel pumps," *IEEE Trans. Ind. Appl*., vol. 39, no. 6, pp. 1734–1740, Nov./Dec. 2003.
[19] W. Li, J. Fang, H. Li, J. Tang, "Position sensorless control without phase shifter for high–speed BLDC motors with low inductance and nonideal back EMF," *IEEE Trans. Power Electron*., vol. 31, no. 2, pp. 1354–1366, Feb. 2016.
[20] H. Li, S. Zheng, and H. Ren, "Self-correction of commutation point for high-speed sensorless BLDC motor with low inductance and non-ideal back EMF," IEEE Trans. Power Electron., vol. 32, no. 1, pp. 642–651, Jan. 2017.
[21] D. Lee, and W. Lee, "Analysis of relationship between abnormal current and position detection error in sensorless controller for interior permanent–magnet brushless dc motors," *IEEE Trans. Magn*., vol. 44, no. 8, pp. 2074–2081, Aug. 2008.
[22] X. Zhou, X. Chen, M. Lu, et al., "Rapid self-compensation method of commutation phase error for low inductance BLDC motor," *IEEE Trans. Ind. Inform*., to be published, doi: 10.1109/TII.2017.2653812.
[23] X. Zhou, X. Chen, M. Lu, et al., "Fast commutation instant shift correction method for sensorless coreless BLDC motor based on terminal voltage information," *IEEE Trans. Power Electron*., to be published, doi: 10.1109/TPEL.2017.2661745.
[24] S. Yang, Y. Hsu, "Full speed region sensorless drive of permanent magnet machine combining saliency-based and Back-EMF-based drive," *IEEE Trans. Ind. Electron*., vol. 64, no. 2, pp. 1092–1101, Feb. 2017.
[25] G. Su, and J. McKeever, "Low–cost sensorless control of brushless DC motors using a frequency–independent phase shifter," *IEEE Trans. Power Electron*., vol. 19, no. 2, pp. 296–302, Mar. 2004.
[26] T. Kim, and M. Ehsani, "Sensorless control of BLDC motors from near–zero to high speeds," *IEEE Trans. Power Electron*., vol. 19, no. 6, pp. 1635–1645, Nov. 2004.
[27] R. Chladny and C. Koch, "Flatness–Based tracking of an electromechanical VVT actuator with disturbance observer feed–forward compensation," *IEEE Trans. Control Syst. Technol*., vol. 16, no. 4, pp. 652–663, Jul. 2008.
[28] J. Fang, X. Zhou, and G. Liu, "Instantaneous torque control of small inductance brushless DC motor," *IEEE Trans. Power Electron*., vol. 27, no. 12, pp. 4952–4964, Dec. 2012.
[29] J. Fang, W. Li, and H. Li, "Self–compensation of the commutation angle based on dc–link current for high–speed brushless dc motors with low inductance," *IEEE Trans. Power Electron*., vol. 29, no. 1, pp. 428–438, Jan. 2014.
[30] D. Lee and W. Lee, "Analysis of relationship between abnormal current and position detection error in sensorless controller for interior permanent–magnet brushless DC motors," *IEEE Trans. Magn*., vol. 44, no. 8, Aug. 2008.
[31] J. Cao and B. Cao, "Fuzzy–logic–based sliding–mode controller design for position–sensorless electric vehicle," *IEEE Trans. Power Electron*., vol. 24, no. 10, pp. 2368 – 2378, Oct. 2009.
[32] J. Fang, H. Li, and B. Han, "Torque ripple reduction in BLDC torque motor with noni deal back EMF," *IEEE Trans. Power Electron*., vol. 27, no. 11, pp. 4630–4637, Nov. 2012.
[33] G. Su, and J. McKeever, "Low–cost sensorless control of brushless DC motors with improved speed range," *IEEE Trans. Power Electron*., vol. 19, no. 2, pp. 296–302, Mar. 2004.
[34] J, Fang, X, Zhou, G, Liu, "Precise accelerated torque control for small inductance brushless DC motor," *IEEE Trans. Power Electron.*, vol.28, no.3, pp.1400–1412, Mar. 2013.
[35] S. Chen, G. Liu, L. Zhu, "Sensorless Control Strategy of a 315 kW High-Speed BLDC Motor Based on a Speed-Independent Flux Linkage Function". *IEEE Trans. Ind. Electron*., vol. 64, no. 11, pp. 8607–8617, Nov. 2017.

Shaohua Chen was born in Shandong, China, in 1985. He received the Ph.D. degree in precision instrument and machinery from the Beihang University, Beijing, China, in 2017. He is currently a Lecturer in the School of Instrumentation Science and Opto-Electronics Engineering, Beijing Information Science & Technology University, Beijing, China. His research interests include high-speed permanent magnet motor control, optical fiber sensors, and fiber Bragg grating inscription.

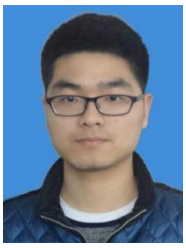

Xiangyu Zhou received the B.S. in automation from Yantai University, Yantai, China, in 2012. He is currently working toward the M.S. degree in Instrument Engineering in the school of Beijing Information Science & Technology University, China. His research interests include high-speed permanent magnet motor control.

Guochang Bai received the B.S. from Henan Polytechnic University (HPU) and M.S. degrees in mechanotronics from Southwest Jiao Tong University (SWJTU), Chengdu, China, in 1991 and 1996, respectively. In 2007, he received the Ph.D. degree in the College of Automation Science and electrical engineering, Beihang University, China. He is currently working in the Institute of mechatronics, Zhengzhou University. His research interests include special motor research and development.

Kun Wang was born in Heilongjiang, China, in 1982. He received the M.Sc. and Ph.D. degrees from the Robotics Institute, School of Mechanical Engineering and Automation, Beihang University (BUAA), Beijing, China, in 2007 and 2011, respectively.
He is currently with the School of Instrumentation Science and Optoelectronics Engineering, Beihang University (BUAA). His main research interests involve the design of the precision instrument and machinery, active magnetic bearing design, high-speed electric machine design, and wall-climbing robot research.

Lianqing Zhu was born in Lanxi, China, in 1963. He received the B.S. and M.S. degrees from Hefei University of Technology, China, in 1984 and 1989. Since 2004, he has been a Professor with the School of Instrumentation Science and Opto-electronics Engineering, Beijing Information Science & Technology University, China. He was elected twelfth members of the CPPCC National Committee in 2013. He was also the leader of Yangtze River Scholars Innovation Team, National Key Talent, National Outstanding Mid-Aged Expert, and Science and Technology Beijing Leader Talent. His research interests include optical fiber sensing and fiber laser, biomedical detection technology and instrument, and precision measurement.

0885-8993 (c) 2017 IEEE. Personal use is permitted, but republication/redistribution requires IEEE permission. See http://www.ieee.org/publications_standards/publications/rights/index.html for more information.